



Contents lists available at ScienceDirect

## Chemical Engineering Journal

journal homepage: [www.elsevier.com/locate/cej](http://www.elsevier.com/locate/cej)

# FeS<sub>2</sub>@N-C nanorattles encapsulated in N/S dual-doped graphene/carbon nanotube network composites for high performance and high rate capability anodes of sodium-ion batteries

Syam Kandula<sup>a</sup>, Beom Sik Youn<sup>b</sup>, Jinhan Cho<sup>c,d</sup>, Hyung-Kyu Lim<sup>b,\*</sup>, Jeong Gon Son<sup>a,d,\*</sup>

<sup>a</sup> Soft Hybrid Materials Research Center, Korea Institute of Science and Technology, 5 Hwarang-ro 14-gil, Seongbuk-gu, Seoul 02792, Republic of Korea

<sup>b</sup> Division of Chemical Engineering and Bioengineering, Kangwon National University, Chuncheon, Gangwon-do 24341, Republic of Korea

<sup>c</sup> Department of Chemical and Biological Engineering, Korea University, Seoul 02841, Republic of Korea

<sup>d</sup> KU-KIST Graduate School of Converging Science and Technology, Korea University, 145 Anam-ro, Seongbuk-gu, Seoul 02841, Republic of Korea

## ARTICLE INFO

## Keywords:

Iron sulfide (FeS<sub>2</sub>)  
Graphene/CNT  
Sodium-ion batteries  
Anode material  
Energy storage  
Specific capacity

## ABSTRACT

Developing effective anode materials for sodium-ion batteries (SIBs) remains challenging. Although FeS<sub>2</sub> has a high theoretical capacity, it suffers from significant volume changes during charge/discharge and forms soluble polysulfides at lower potentials (below 0.8 V vs. Na/Na<sup>+</sup>), making practical application difficult. We have developed an effective strategy to synthesize N-doped carbon-coated FeS<sub>2</sub> nanorattles encapsulated in N/S dual-doped graphene/single-walled carbon nanotubes (G/SWCNTs) via hydrothermal vulcanization (FSCGS). This approach enabled the simultaneous formation of nanorattle structures and N/S dual-element doping into the G/SWCNT network. Using the FSCGS sample as an anode for SIBs, a remarkable specific capacity of 1,190 mAh g<sup>-1</sup> at a current density of 0.1 A g<sup>-1</sup> was achieved, with an excellent rate capability of 476 mAh g<sup>-1</sup> at 10.0 A g<sup>-1</sup>. Moreover, it exhibited superior cyclic stability, with a capacity retention of 91.3% at 0.5 A g<sup>-1</sup> after 200 cycles. First-principles calculations revealed that pyridinic-N/S doping of the basal graphene network improved Na<sup>+</sup> reduction, resulting in enhanced electrochemical performance. The effective electrochemical functioning of the FSCGS anode material was attributed to an optimized hierarchical architecture and the excellent electrical conductivity/electrochemical activity provided by the dual carbon entities (N-doped carbon and N/S dual-doped G/SWCNT network).

## 1. Introduction

By supporting the digital arena and technological developments toward electrification of vehicles, energy storage devices have become vital for our daily lives [1,2]. Consequently, extensive research has been devoted to developing efficient energy storage devices, such as lithium (Li)-ion batteries (LIBs), sodium (Na)-ion batteries (SIBs), and potassium (K)-ion batteries to make this possible [3–9]. Among these, SIBs are of particular interest because of the high natural abundance of Na, which would reduce the fabrication cost for commercial use in many practical applications [10–12], including transportation, grid-level applications, defense, and aerospace [13,14]. However, the atomic radius of Na<sup>+</sup> is 1.34-times larger than that of Li<sup>+</sup>, [15–17] making it challenging to intercalate into graphite (a typical Li-ion anode material), which limits

practical applications [18,19]. Furthermore, the larger radius of Na<sup>+</sup> results in massive volume expansion of electrodes during charge/discharge, resulting in electrode pulverization and degeneration [20–22]. Therefore, designing a suitable anode host with excellent specific capacity and energy density is essential to mitigate pulverization during charge/discharge.

Various carbonaceous materials and metal oxides/sulfides/phosphides have been explored as anode materials for SIBs [19,23–29]. Carbonaceous materials exhibit huge irreversible capacity loss and ambiguous potential windows, leading to poor rate capability. Conversely, metal oxides/sulfides/phosphides suffer from significant volume expansion, and material degeneration causes inferior electrochemical performance. Metal sulfides are of interest because of their high theoretical capacity [30,31]. Particularly, iron sulfide (FeS<sub>2</sub>) is

\* Corresponding authors at: Soft Hybrid Materials Research Center, Korea Institute of Science and Technology, 5 Hwarang-ro 14-gil, Seongbuk-gu, Seoul 02792, Republic of Korea (Jeong Gon Son). Division of Chemical Engineering and Bioengineering, Kangwon National University, Chuncheon, Gangwon-do 24341, Republic of Korea (Hyung-Kyu Lim).

E-mail addresses: [hklim@kangwon.ac.kr](mailto:hklim@kangwon.ac.kr) (H.-K. Lim), [jgson@kist.re.kr](mailto:jgson@kist.re.kr) (J. Gon Son).

<https://doi.org/10.1016/j.cej.2022.135678>

Received 1 December 2021; Received in revised form 26 January 2022; Accepted 5 March 2022

Available online 8 March 2022

1385-8947/© 2022 The Authors.

Published by Elsevier B.V. This is an open access article under the CC BY-NC license

(<http://creativecommons.org/licenses/by-nc/4.0/>).

environmentally benign, intrinsically safe, naturally abundant, and has a high theoretical capacity ( $894 \text{ mAh g}^{-1}$ ) [32,33]. The marcasite  $\text{FeS}_2$  (m- $\text{FeS}_2$ ) possesses a lower bandgap (0.40 eV) than pyrite  $\text{FeS}_2$  (p- $\text{FeS}_2$ ) (0.95 eV), demonstrating better electrical conductivity in m- $\text{FeS}_2$  [34]. However, the metastable nature and typical synthetic procedure of m- $\text{FeS}_2$  restrict its exploration towards practical energy storage. Therefore, p- $\text{FeS}_2$  has been explored as a LIB and SIB anode material. It undergoes intercalation and conversion reactions during charge/discharge, similar to transition-metal sulfides [35,36]. However, p- $\text{FeS}_2$  stores energy via a diffusive mechanism rather than capacitive charge storage, accompanied by sluggish kinetics, resulting in inferior electrochemical performance [32,36]. Moreover, p- $\text{FeS}_2$  suffers from poor electrical conductivity and displayed significant volume expansion (280%) during cyclic stability testing [37,38].

Various strategies have been explored to overcome these issues [19,32,38–43]. One approach has been to close the potential window at 0.8 V, resulting in improved cyclic stability. However, this sacrifices reversible capacity and energy density, which is a major barrier to practical applications [32,39,40]. For better rate capability and cyclic stability, tuning the  $\text{FeS}_2$  particle size from micro- to nanosized has been proposed using foam-like nanoparticle aggregates [38] and nanoparticles embedded in a micro-sized carbon matrix [42]. However, nanoparticle-based materials typically experience low tap density and initial Coulombic loss, which are major concerns for practical applications. To accommodate the volume expansion of  $\text{FeS}_2$ , yolk@shell materials have been suggested as anodes for SIBs. Carbon-encapsulated  $\text{FeS}_2$  ( $\text{FeS}_2$ @C) yolk@shell nanoboxes demonstrated better cyclic stability with improved specific capacity than fully occupied  $\text{FeS}_2$ @C nanoboxes [41] but still exhibited lower specific capacity [39]. To improve the conductivity of  $\text{FeS}_2$ , integration with highly conductive graphene networks was performed; [19,40], which provided better cyclic stability but low specific capacity. Heteroatom doping to carbon shells has also been studied and provided good specific capacity but poor rate performance and cycle stability [43]. Recently, Hao et al. have explored dual crystalline  $\text{FeS}_2$  towards  $\text{Na}^+$  storage and observed that volume expansion was controlled by asynchronous reactions of “self-matrix” effect of dual crystalline  $\text{FeS}_2$  [44]. Extensive research has focused on efficient  $\text{FeS}_2$ -based anode materials for SIBs, but achieving superior cyclic stability, specific capacity, and rate capability simultaneously remains a challenge.

Herein, we demonstrate a novel structure encapsulating  $\text{FeS}_2$ @N-C nanorattles in an N/S dual-doped graphene/single-walled carbon nanotube (G/SWCNT) network composite prepared via a one-step hydrothermal approach. Here, the high conductivity and nanometer-thick graphene and SWCNTs tightly and thoroughly attach to the  $\text{FeS}_2$ @N-C nanorattles, providing highly conductive multiple pathways and preventing the agglomeration of the nanorattles, playing crucial role in improving the electrical transport within the FSCGS composites, which is a drawback of core-shell or nanorattle structures. The synthesized hierarchical architecture was optimized for energy storage as follows: nanorattle structures accommodating significant volume changes; N-doped carbon coating over  $\text{FeS}_2$  protecting from direct interaction with electrolyte; highly conductive graphene/SWCNT network providing multiple electrical highways and high surface area; and pyridinic-N/S doping into G/SWCNT network enhancing the carrier density and facilitating  $\text{Na}^+$  diffusion. As a result, the multi-featured  $\text{FeS}_2$ @N-C nanorattles, encapsulated in an N/S dual-doped G/SWCNT network composite electrode as an anode for SIBs, demonstrated a remarkable specific capacity of  $1,190 \text{ mAh g}^{-1}$  at a current density of  $0.1 \text{ A g}^{-1}$ , along with excellent rate capability ( $476 \text{ mAh g}^{-1}$  at  $10.0 \text{ A g}^{-1}$ ). Moreover, it exhibited specific capacity retention of 91.3% at  $0.5 \text{ A g}^{-1}$  and 83.6% at  $1.0 \text{ A g}^{-1}$  after 200 cycles in the large potential window of 0.005–3.0 V vs.  $\text{Na}/\text{Na}^+$ . Through first-principles calculations, we investigated the theoretical background for the performance improvement derived from changes in Na overpotential and differences in partial charge due to N/S doping in graphene networks. As a result, we

successfully implemented the optimized architecture and enlarged the working potential window, resulting in superior specific capacity and rate capability along with significantly improved cyclic stability, which are vital characteristics for practical SIB applications.

## 2. Results and discussion

A schematic representation of the synthesis of  $\text{FeS}_2$ @N-C nanorattles encapsulated in an N/S dual-doped graphene/SWCNT network composite (FSCGS) is presented in Fig. 1. The reaction between  $\text{Fe}_2\text{O}_3$  nanocubes and dopamine hydrochloride at room temperature in Tris-HCl buffer resulted in a uniformly coated polydopamine (PDA) layer on the surface of  $\text{Fe}_2\text{O}_3$  nanocubes. Calcination of  $\text{Fe}_3\text{O}_4$ @PDA at high temperature under argon atmosphere produced  $\text{Fe}_3\text{O}_4$ @N-C core@shell. The  $\text{Fe}_3\text{O}_4$ @N-C core@shell nanocubes were mixed in a graphene oxide (GO; 36 mg) aqueous solution, tip-sonicated for uniform dispersion, and combined with a tip-sonicated SWCNT (15 mg) dispersion. Quenching of the  $\text{Fe}_3\text{O}_4$ @N-C core@shell nanocubes in the GO/SWCNT dispersion in liquid nitrogen, followed by freeze-drying, encapsulated the  $\text{Fe}_3\text{O}_4$ @N-C core@shell nanocubes into the GO/SWCNT network. Finally, hydrothermal sulfurization with thioacetamide at  $200^\circ\text{C}$  for 6 h formed  $\text{FeS}_2$ @N-C nanorattles encapsulated in an N/S dual-doped graphene/SWCNT (mass ratio 1.5:1) network (FSCGS) composite. The formation of nanorattle structures can be explained by Ostwald ripening [45,46].

Various characterization techniques were used to confirm the formation of pure  $\text{FeS}_2$  nanoparticles (FS),  $\text{FeS}_2$ @N-C nanorattles (FSC), and the FSCGS network. Initially, the morphology of all of the samples was examined using field-emission scanning electron microscopy (FE-SEM). Transmission electron microscopy (TEM) was then carried out to explore the FSCGS sample. The FE-SEM image of  $\text{Fe}_3\text{O}_4$ @N-C shows a uniform coating of carbon shells over the surface of  $\text{Fe}_3\text{O}_4$  nanocubes, and the mean diameter was estimated to be about  $550 \pm 10 \text{ nm}$  (Fig. 2a). The FE-SEM image of pure  $\text{FeS}_2$  shows aggregated nanoparticles (Fig. 2b), and the size of the nanoparticles was estimated to be about  $100 \pm 20 \text{ nm}$ . The FE-SEM image of  $\text{FeS}_2$ @N-C shows an aggregated FS core with transparent carbon shells (Fig. 2c); here, the carbon coating is protected from the aggregation of FS. Fig. 2d illustrates the uniform distribution of  $\text{FeS}_2$ @N-C nanorattles in a network of N/S dual-doped G/SWCNT. The TEM images of the FSCGS sample clearly show a void space between the FS and N-C shell, indicating the formation of FSC structures (Fig. 2e and f). In addition, the images offer the wrapping of graphene layers and SWCNTs over the surface of the FSC. The high-resolution TEM image indicates a clear interface between the graphene, carbon, and  $\text{FeS}_2$  (Fig. 2g), with a lattice spacing of 0.54 nm consistent with the (100) plane of p- $\text{FeS}_2$ . The selected area electron diffraction pattern demonstrates the polycrystalline nature of  $\text{FeS}_2$  (Fig. 2h) and indicates diffractions corresponding to the dual phases of p- and m- $\text{FeS}_2$ . The FE-SEM images of FSCG and FSCS samples are shown in Fig. S1. The elemental composition and color mapping of FS, FSC, and FSCGS samples were analyzed using energy-dispersive X-ray spectroscopy (EDS) coupled with FE-SEM (Figs. S2–S4). The EDS color mapping further confirmed the formation of  $\text{FeS}_2$  in all three samples. Notably, Figure S3 shows intense colors corresponding to S and N throughout the sample, suggesting the doping of N and S into the G/SWCNT network. The TEM-EDS color mapping further indicated the presence of required elements, suggesting the formation of FSC encapsulated into the N/S dual-doped G/SWCNT network composite (Fig. 2i–n).

The phase purity of all of the samples was examined using XRD analysis, which confirmed the formation of p- $\text{FeS}_2$  (JCPDS no: 42–1340) (major contribution) and m- $\text{FeS}_2$  (JCPDS no: 37–0475) (minor contribution) (Fig. S5a). The presence of a minor percentage of m- $\text{FeS}_2$  in the FSC may boost electrical conductivity and ensure the structural integrity of FSC. However, no reflections due to carbon or G/SWCNT were observed in the XRD patterns of the FSC and FSCGS samples. To confirm the presence of carbon or G/SWCNT in these samples, we conducted a non-destructive Raman spectroscopy analysis (Fig. 3a). All three

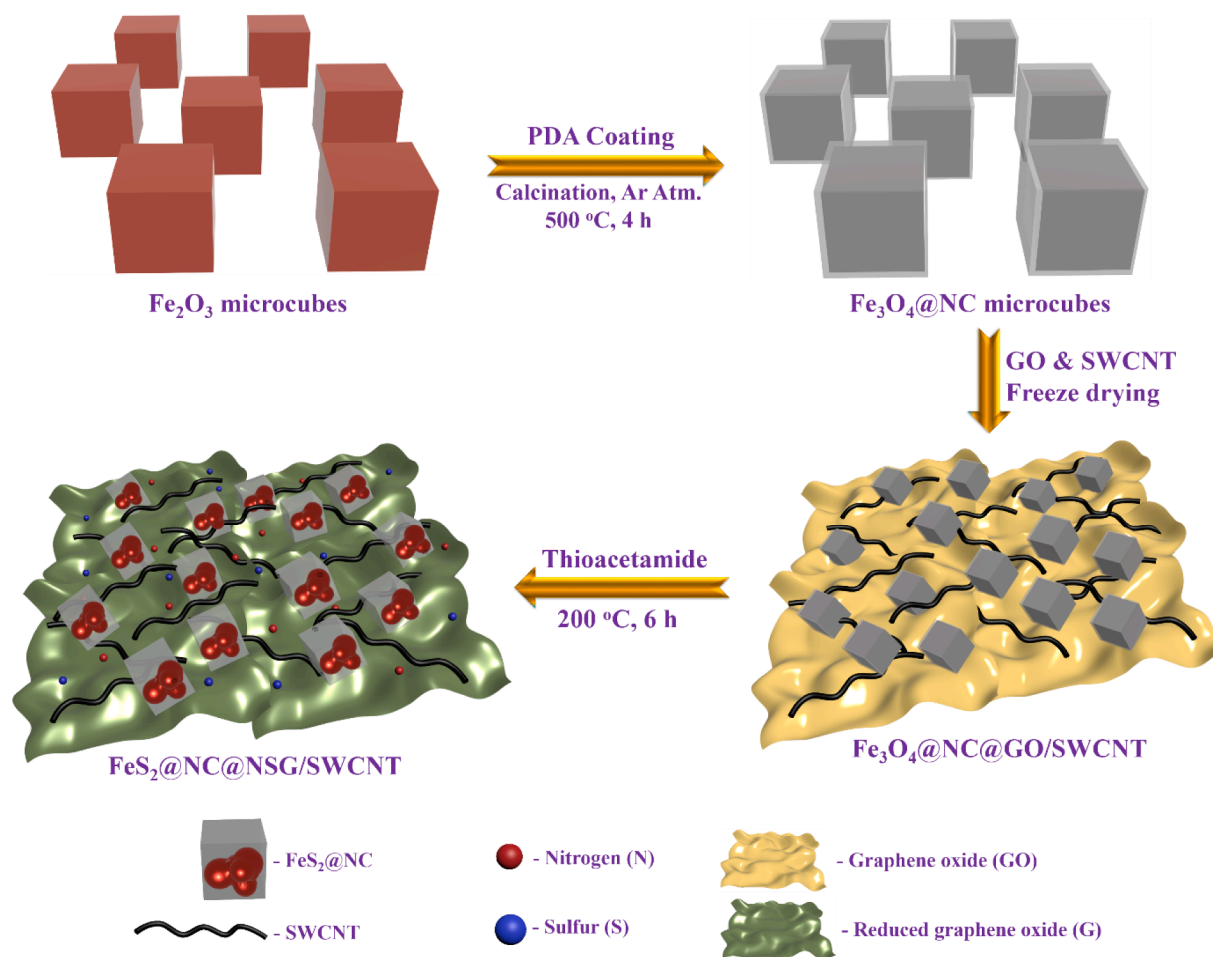


Fig. 1. Schematic representation of the synthesis of  $\text{FeS}_2@\text{N-C}$  nanorattles encapsulated in an N/S dual-doped graphene/SWCNT network.

samples (FS, FSC, and FSCGS) displayed Raman vibrations at 320, 335, 380, and 433  $\text{cm}^{-1}$ . Among them, the Raman vibration at 320  $\text{cm}^{-1}$  is consistent with the  $A_g$  characteristic mode of m- $\text{FeS}_2$  [34,47]. The other three vibrations, at 335, 380, and 433  $\text{cm}^{-1}$ , are attributed to  $E_g$  (out-of-plane displacement of S atoms),  $A_g$  (in-plane S-S stretching), and  $T_g$  (symmetry mode), respectively, of p- $\text{FeS}_2$  [48,49]. The GS, FSC, and FSCGS samples showed two additional Raman vibrations at 1,330 and 1,590  $\text{cm}^{-1}$ , corresponding to the D and G bands of carbon or G/SWCNT [39,50]. The GS sample showed a broad D band with an intense G band ( $I_D/I_G = 0.5$ ), indicating the presence of  $\text{sp}^2$ -hybridized graphene/CNT. The FSC sample showed an intense broad D band and weak G band ( $I_D/I_G = 3.9$ ), indicating more defective and less graphitized carbon with the presence of a short-range graphitic structure in the N-C shell [50,51]. In contrast, the FSCGS sample displayed a highly intense G band compared with the D band ( $I_D/I_G = 0.1$ ) because of the high content of  $\text{sp}^2$ -hybridized graphene/CNT materials [43]. The Raman analysis further confirmed the co-existence of p- and m- $\text{FeS}_2$  and highly graphitized carbon in the FSCGS sample.

The  $\text{FeS}_2$  content of the FSC and FSCGS samples determined by thermogravimetric analysis under air atmosphere was 94.0% and 84.0%, respectively (Fig. S5b). Pore size distribution and specific surface area (SSA) studies were also carried out (Fig. S6). All of the samples (FS, FSC, and FSCGS) displayed a type-IV curve with H3 hysteresis, which indicated the presence of mesopores (Figs. S6a-c). The SSA of FS, FSC, and FSCGS was estimated as 40.8, 68.0, and 94.2  $\text{m}^2 \text{g}^{-1}$ , respectively. The presence of atomically thin G/SWCNT in the FSCGS sample enhanced the surface area, providing additional active sites for better  $\text{Na}^+$  storage. The pore size, derived from Barrett-Joyner-Halenda analysis, was less than 2.0 nm for all samples, indicating the presence of

distinct mesopores; these are vital for  $\text{Na}^+$  storage (Fig. S6d).

The surface oxidation states and composition of the FS, FSC and FSCGS samples were assessed using X-ray photoelectron spectroscopy (XPS). Fig. S7 displays the survey spectra of the FSCGS sample, and the XPS spectra of FS and FSC samples are shown in Figs. S8 and S9, respectively. The high-resolution Fe 2p spectrum displayed two characteristic peaks at 707.1 and 719.8 eV, corresponding to Fe 2p<sub>3/2</sub> and Fe 2p<sub>1/2</sub> doublet splitting due to spin-orbit coupling of  $\text{FeS}_2$  (Fig. 3b) [34,40]. The high-resolution S 2p spectrum was deconvoluted into several peaks (Fig. 3c). The peaks at 162.5 and 164.8 eV correspond to Fe-S 2p<sub>3/2</sub> and Fe-S 2p<sub>1/2</sub>, respectively, and another peak at 163.6 eV relates to C-S 2p<sub>3/2</sub>, indicating S doping into the G/SWCNT network [52]. The C 1s spectrum was deconvoluted into four peaks corresponding to C-C/C=C (284.5 eV), C-N (285.1 eV), C-S (286.3 eV), and O-C=O (288.4 eV) bonds, indicating successful doping of N/S into the G/SWCNT network (Fig. 3d) [43,52]. The electron-rich donors (pyridinic N/S) co-doped into the G/SWCNT network improved charge carrier density, thus enhancing electrical conductivity via improved charge kinetics [40]. The N 1s spectrum comprised three peaks corresponding to relatively strong pyridinic N (398.3 eV) (compared with the FSC sample), pyrrolic N (399.9 eV), and graphitic N (401.4 eV) (Fig. 3e) [43,52]. Pyridinic N can introduce defects into the G/SWCNT network, resulting in more active sites for  $\text{Na}^+$  insertion and extraction (supported by the later theoretical analysis) [51]. Therefore, the N content of the FSC and FSCGS samples was estimated as 3.4 and 5.8 at%, respectively, indicating higher N content in the FSCGS sample. The high-resolution O 1s spectra showed three peaks centered at 530.9, 531.7, and 532.9 eV, corresponding to O-Fe, O-C, and O-C=O bonds (Fig. 3f) [25]. These results further support the formation of FSC encapsulated into N/S dual-

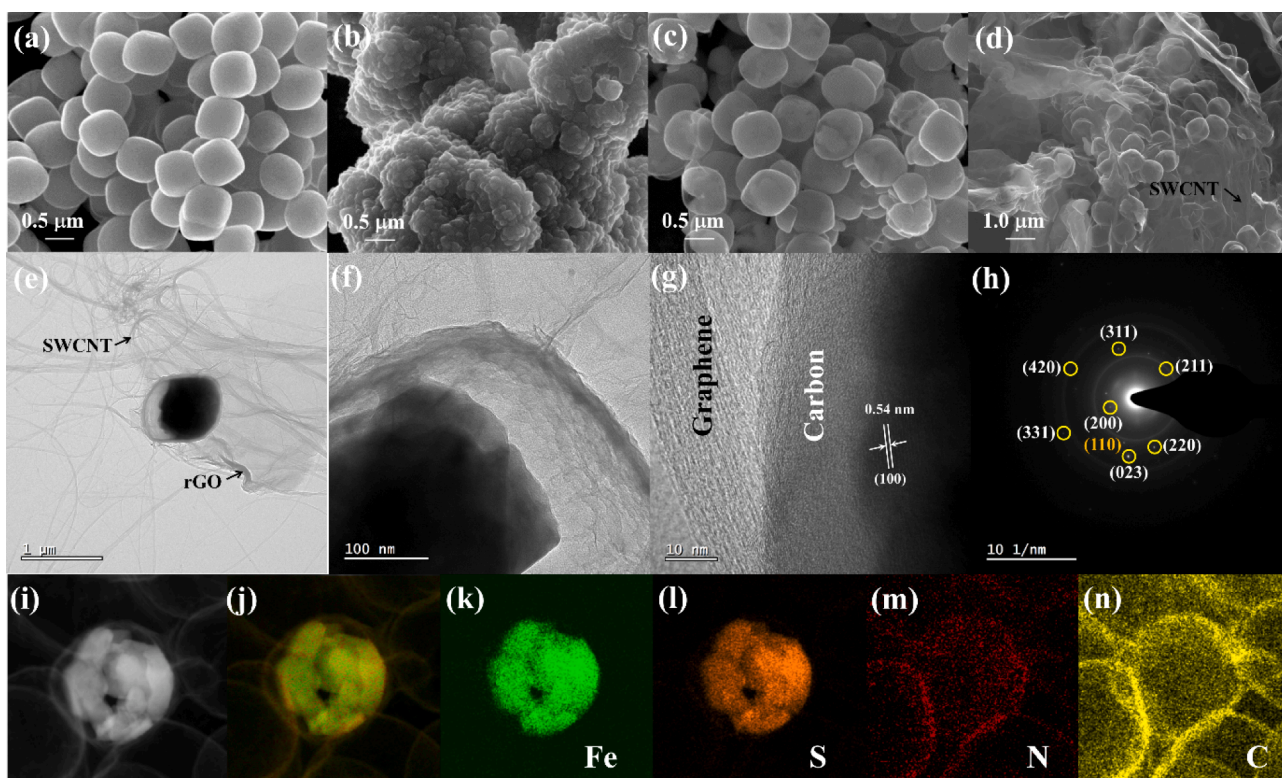


**Fig. 2.** (a-c) Field-emission scanning electron microscopy (FE-SEM) images of the Fe<sub>3</sub>O<sub>4</sub>@C, FS, and FSC samples. (d) FE-SEM, (e, f) transmission electron microscopy (TEM), (g) high-resolution TEM, (h) selected area electron diffraction, and (i-n) energy-dispersive X-ray spectroscopy color mapping of the FSCGS sample.

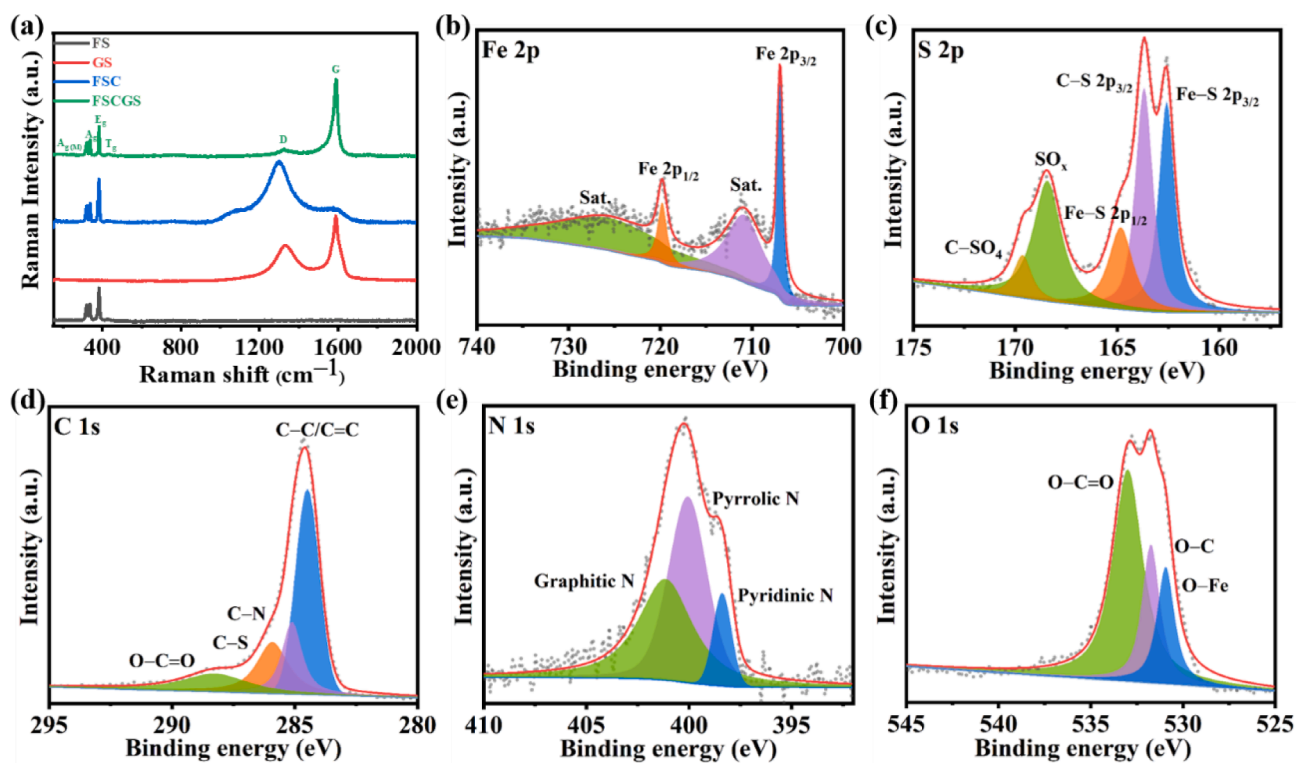
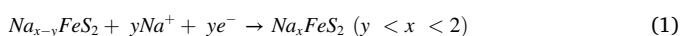


**Fig. 3.** (a) Raman spectra of the FS, GS, FSC, and FSCGS samples. High-resolution X-ray photoelectron spectra of the (b) Fe 2p, (c) S 2p, (d) C1s, (e) N1s, and (f) O 1s regions of the FSCGS sample.

doped G/SWCNT network composites.

To understand the effect of  $\text{Na}^+$  storage on the unique structural features of the FSCGS sample compared with the FS and FSC samples, we evaluated each sample as an anode for SIBs. It is established that electrolyte solvents and salts play crucial roles in electrode performance, especially for metal sulfides. Based on the experimental results for suitable electrolyte solvents (Fig. S10) and salts (Fig. S11) for higher voltage windows, we chose 1.0 M  $\text{NaClO}_4$  in diglyme with 10.0 vol% fluoroethylene carbonate for electrochemical tests. Cyclic voltammetry (CV) analysis of the FS, FSC, and FSCGS samples was conducted using a potential window of 0.005–3.0 V vs.  $\text{Na}/\text{Na}^+$  at a scan rate of  $0.2 \text{ mV s}^{-1}$ ; the corresponding first cycle CV results are shown in Fig. S12a (the first cycle analyses are described in the Supporting Information.). After the first cycle, the electrode kinetics of all samples was verified at a scan rate of  $0.2\text{--}1.0 \text{ mV s}^{-1}$  (Fig. 4a, Figs. S12b, and S12c). All of the samples exhibited a new cathodic peak at 2.0 V vs.  $\text{Na}/\text{Na}^+$ , with the disappearance of the cathodic peak near about 0.8 V vs.  $\text{Na}/\text{Na}^+$ , indicating Na insertion at higher voltage; this can be expressed according to Eq. (1), as follows [38]:



The FSCGS sample showed prominent redox peaks with a higher area under the CV curve at all scan rates than the FS and FSC samples (Fig. 4a), indicating excellent electrode kinetics and faster diffusion of  $\text{Na}^+$  ions during insertion and extraction via the N/S dual-doped G/SWCNT network. To understand the improved electrochemical performance of the FSCGS sample, the charge-storage mechanism was evaluated according to Eqs. (2) and (3) as follows [39,40]:

$$i = av^b \quad (2)$$

$$\log i = \log a + b \log v \quad (3)$$

Plots of a  $\log v$  as a function of  $\log i$  showed a linear relationship for all samples (Figs. S12d–f). Among them, the slope of the FSCGS sample was much greater than 0.5 for all of the peaks (Fig. S12f), suggesting a significant charge contribution from capacitive charge storage ( $b = 1.0$ ) rather than the ion-diffusion process ( $b = 0.5$ ) [25,53]. The impact of the

capacitive and ion-diffusion processes in these samples was enumerated according to Eq. (4), as follows [25,39].

$$i(V) = k_1v + k_2v^{1/2} \quad (4)$$

The charge contribution at various scan rates for all samples is shown in Fig. 4b. The FS sample showed a significant charge contribution from the ion-diffusion controlled process (85.0% at  $1.0 \text{ mV s}^{-1}$ ) rather than capacitive charge storage, indicating ion diffusion-dominated electrode kinetics. In the FSC sample, the capacitive and ion-diffusion contribution was almost 50:50, demonstrating improved capacitive charge input compared with pure  $\text{FeS}_2$ . In the FSCGS sample, the capacitive charge contribution was 73.0% at  $1.0 \text{ mV s}^{-1}$ , showing enhanced capacitive charge input offered by oxygen-functional groups (OFS) present in N/S dual-doped G/SWCNT network in the FSCGS sample, and thus excellent electrochemical performance compared with the FS and FSC samples. The presence of OFS, especially carbonyl ( $\text{C}=\text{O}$ ) and carboxyl ( $\text{COOH}$ ) groups, act as redox-active sites, which can store the Na-ion via a faster charge storage kinetics [54]. Moreover, OFS can also help enlarge the interlayer distance, create more active sites, and promote faster charge transfer in the N/S dual-doped G/SWCNT network, resulting in improved specific capacity in the FSCGS sample [55].

Galvanostatic charge–discharge (GCD) analysis was carried out to verify the exemplary electrochemical behavior of the FSCGS sample compared with the FS, FSC, FSCG, and FSCS samples (Fig. 4c and Fig. S13). The discharge and charge specific capacities in the first cycle for the FS, FSC, and FSCGS samples, at a current density of  $0.1 \text{ A g}^{-1}$ , were 1,393.3 and 776.1, 955.9 and 547.8, and 1,848.7 and 1,122.5  $\text{mAh g}^{-1}$ , respectively. The corresponding Coulombic efficiencies were 55.7, 57.3, and 60.7%. The discharge capacity in the next cycle at the same current density was 807.5, 553.6, and 1,188.9  $\text{mAh g}^{-1}$  for the FS, FSC, and FSCGS samples, respectively. A capacity loss between the first two cycles occurred due to forming a stable solid electrolyte interphase (SEI) layer and intercalation of Na into the crystal lattice of  $\text{FeS}_2$  [19,25,43]. The high discharge capacity of the FSCGS sample is attributed to the contribution of specific capacity offered by  $\text{FeS}_2$  and dual carbon entities. Afterward, to enumerate the rate capability of the samples, GCD was carried out at various current densities between 0.1 and  $10.0 \text{ A g}^{-1}$

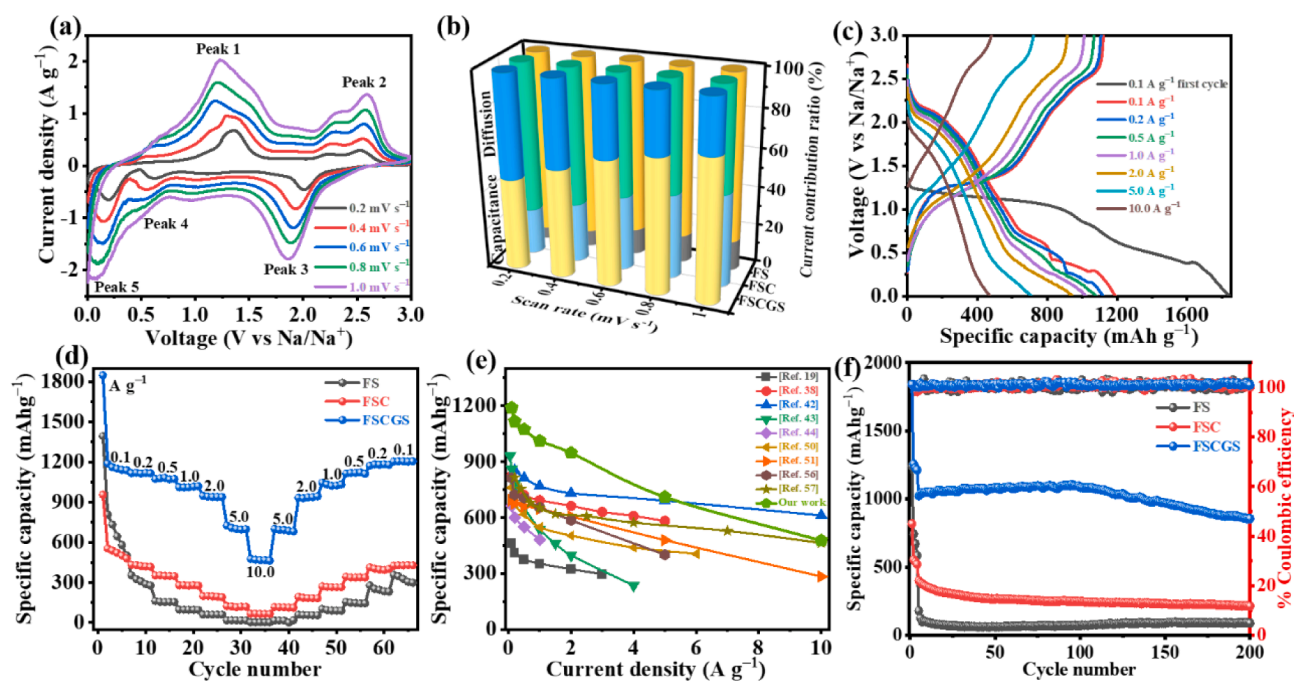


Fig. 4. (a) Cyclic voltammetry spectra of the FSCGS samples at different scan rates. (b) Current contribution ratio plots of the FS, FSC, and FSCGS samples. (c) Galvanostatic charge–discharge plots of the FSCGS sample. (d) Rate capability plots of the FS, FSC, and FSCGS samples. (e) Comparison of specific capacity at different current densities with literature data. (f) Cyclic stability plots of the FS, FSC, and FSCGS samples at  $1.0 \text{ A g}^{-1}$  for 200 cycles.

(Fig. 4d). The measured discharge capacities of the FS and FSC samples were 276.6, 153.4, 95.0, 59.5, 16.7, and 3.2 mAh g<sup>-1</sup> and 417.0, 347.4, 276.8, 190.1, 119.0, and 64.6 mAh g<sup>-1</sup> at 0.2, 0.5, 1.0, 2.0, 5.0, and 10.0 A g<sup>-1</sup>, respectively. The FS sample showed rapid capacity fading in the initial cycles at 0.1 A g<sup>-1</sup>, indicating the development of a fresh SEI layer in each cycle due to direct exposure of FeS<sub>2</sub> with the electrolyte [25]. The FS and FSC samples retained only 36.9% and 77.3% of their initial capacities when returning to 0.1 A g<sup>-1</sup>, indicating large capacity loss due to the formation of soluble polysulfide in the electrolyte. The discharge capacities of the FSCGS sample were 1,115.7, 1,073.9, 1,019.7, 947.2, 710.3, and 476.5 mAh g<sup>-1</sup> at the same current densities. Upon returning the current density to 0.1 A g<sup>-1</sup>, the FSCGS sample exhibited a discharge capacity of about 1,205.9 mAh g<sup>-1</sup>, slightly higher than the initial discharge capacity. Moreover, it exhibited a higher specific capacity (~107.4%) than at initial cycles, indicating stable SEI formation and reduced polysulfide dissolution during the rate capability test. Fig. 4e compares the specific capacities at various current densities of the FSCGS sample with literature data (Table S1). It reveals extraordinary specific capacities compared with previously reported FeS<sub>2</sub>-based materials until 5.0 A g<sup>-1</sup>, and comparable specific capacity at 10.0 A g<sup>-1</sup> [19,38,42–44,50,51,56,57]. The previously reported tapped densities & Coulombic efficiencies of nano-embedded microstructured FeS<sub>2</sub>@C of 15 nm (1.4 g cm<sup>-3</sup> & 84.7 %) [42], pitaya-structured p-FeS<sub>2</sub> of 200 nm (1.3 g cm<sup>-3</sup> & 90.0 %) [58], H-MoS<sub>2</sub> nanosheets (0.8 g cm<sup>-3</sup> & 75.0 %) [59], p-FeS<sub>2</sub> microspheres of 3 μm (2.2 g cm<sup>-3</sup> & 71.4 %) [32], and FeSe<sub>2</sub> microspheres of 5 μm (1.85 g cm<sup>-3</sup> & 88.0 %) [60], respectively. The FSCGS sample shows tapped density of 2.19 g cm<sup>-3</sup> with a Coulombic efficiency of 60.7%. It demonstrates better tap density with comparable Coulombic efficiency.

The cyclic stability of three samples was assessed at a current density of 1.0 A g<sup>-1</sup> for 200 cycles (Fig. 4f). The FS sample underwent rapid discharge capacity decay during the first 10 cycles and stabilized at about 100.0 mAh g<sup>-1</sup> until 200 cycles. The rapid capacity deterioration during the first 10 cycles is attributed to the electrolyte decomposition of a stable SEI layer during the initial cycles. The FSC sample also showed capacity fading during the initial 100 cycles and then exhibited slow capacity decay in the subsequent 100 cycles. In contrast, the FSCGS sample displayed increased discharge capacity from 1,023 to 1,096 mAh g<sup>-1</sup> until 100 cycles. The enhancement in discharge capacity during the first 100 cycles is attributed to the activation process of FeS<sub>2</sub>, which could be due to the improved electrical conductivity offered by the synergistic interaction between the N/S dual-doped highly graphitized G/SWCNT network and N-C shell [38,50]. However, there was a decreasing trend in discharge capacity over the subsequent 100 cycles, where it reached about 855.9 mAh g<sup>-1</sup> with retention of 83.6% of its initial capacity. The decreasing trend of specific capacity can be attributed to the formation and establishment of a stable SEI layer by inferential decomposition of electrolyte; also the occurrence of irreversible reactions between Na<sup>+</sup> and residual oxygen functional groups of PDA-derived carbon, as well as rGO derived graphene [41,50]. We also tested the FSCGS sample's cyclic stability at 0.5 A g<sup>-1</sup> for 200 cycles and at 5.0 A g<sup>-1</sup> for 1,000 cycles (Figs. S14a and S14b). At 0.5 A g<sup>-1</sup>, a similar trend was observed to that at 1.0 A g<sup>-1</sup>, and about 91.3% (964.7 mAh g<sup>-1</sup>) of its initial capacity (1,056.9 mAh g<sup>-1</sup>) was retained.

To understand the capacity decay as a function of cycles in the three samples, we examined the morphology of the cells after different numbers of cycles using FE-SEM (Figs. S15 and S16). FE-SEM images of fresh electrodes and electrodes after 20 cycles at 1.0 A g<sup>-1</sup> are shown in Fig. S15. The FS sample showed a large aggregation of FeS<sub>2</sub> particles (Fig. S15b). At the same time, the FSC sample also lost its nanorattles morphology (Fig. S15d), suggesting an interaction of the active component with the electrolyte and subsequent capacity fading. In contrast, the FSCGS sample accommodated the volume change of FeS<sub>2</sub>@NC from 0.7 μm to 0.9 μm during the cycling. The NC shell protects the FeS<sub>2</sub> nanoparticles aggregation and significant expansion at this stage. Moreover, it retained the FSC morphology and was tightly

encapsulated into an N/S dual-doped G/SWCNT network, resulting in enhanced capacity due to the FeS<sub>2</sub> activation process (Fig. S15f). These results suggest a crucial role of the N-C shell, with an N/S dual-doped G/SWCNT network, in boosting the electrochemical performance of FeS<sub>2</sub>.

The enhanced electrochemical behavior of the FSCGS sample compared with the FS and FSC samples were evaluated using electrochemical impedance spectroscopy to understand the electrode kinetics after 200 cycles at 1.0 A g<sup>-1</sup>; the Nyquist plot is presented in Fig. 5a. The equivalent circuit model is shown in the inset of Fig. 5a, and the required parameters were assessed by fitting the curve to the model. The ohmic resistance (R<sub>s</sub>) from the electrode and electrolyte was estimated as 7.0, 5.5, and 3.7 Ω, and the charge-transfer resistance (R<sub>ct</sub>) was calculated as 769.1, 518.3, and 370.6 Ω for the FS, FSC, and FSCGS samples, respectively. These results suggest that the FSCGS sample experienced lower R<sub>s</sub> and R<sub>ct</sub>, indicating that faster electron transfer was enabled by the N/S dual-doped, highly graphitized G/SWCNT network. In addition, the FSCGS sample exhibited a better slope in the low-frequency region than the FS and FSC samples, indicating better Na<sup>+</sup> diffusion via the defective active sites provided by electron-rich dopants in the G/SWCNT network.

The Na<sup>+</sup> diffusion coefficient of the three samples was determined using the galvanostatic intermittent titration technique; the results for the FSCGS sample are shown in Fig. 5b, and those for the FS and FSC samples are shown in Figs. S17a and S17b, respectively. According to Fick's second law, the Na<sup>+</sup> diffusion coefficient was evaluated [25,28]. The plot of τ<sup>1/2</sup> vs V (V vs Na/Na<sup>+</sup>) shows a linear relationship (Fig. S17c). Fig. 5c plots the chemical diffusion of Na<sup>+</sup> as a function of voltage for the three samples, which was estimated as 8.2 × 10<sup>-12</sup> to 7.2 × 10<sup>-10</sup>, 1.9 × 10<sup>-11</sup> to 8.9 × 10<sup>-10</sup>, and 6.8 × 10<sup>-12</sup> to 2.8 × 10<sup>-9</sup> cm<sup>2</sup> s<sup>-1</sup> for the FS, FSC, and FSCGS samples, respectively. These findings indicated better Na<sup>+</sup> diffusion in the FSCGS sample due to defective active sites created by electron-rich dopants in the highly graphitized G/SWCNT network, which improved Na<sup>+</sup> accommodation during the GCD cycles. To further understand the structural transformation in the FSCGS sample during the GCD cycles, *ex-situ* XRD analysis was carried out during the second discharge/charge cycle (Fig. S18). The results indicate that an irreversible phase transformation of FeS<sub>2</sub> into NaFeS<sub>2</sub> occurred during the first cycle. It converted to iron and polysulfide in subsequent discharge cycles and amorphous NaFeS<sub>2</sub> during charging (Fig. 5d). These results suggest that the N-C shell and N/S dual-doped G/SWCNT network could not avoid complete shuttling of polysulfide during the charge/discharge cycles.

First-principles calculations were also performed to determine the origin of the excellent electrochemical performance of the FSCGS sample. Analysis of the experimental results suggests that high contents of N and S doped in the carbon network of the FSCGS composite increased the interaction between Na and the carbonaceous surface. This promoted Na<sup>+</sup> accommodation on the surface, thereby decreasing the overpotential of sodiation. To verify this, sodiation potentials were calculated for each adsorption site on the N- and S-doped basal graphene surface in various doped structures (graphitic, pyridinic, and pyrrolic structures). The basal graphene model was selected because the basal plane occupied a large portion of the microscale FSCGS carbon network.

The Na adsorption sites nearest and farthest from the N and S doping sites were chosen as structurally independent sites; the structurally optimized final adsorption positions, and their binding energies, are shown in Fig. 6a and Table S2, respectively. The Na binding energy was calculated according to the atomic energy of body-centered cubic Na metal and converted into the sodiation potential vs. Na/Na<sup>+</sup> at each site using the Nernst equation (ΔG<sub>B</sub> = -nFE, where ΔG<sub>B</sub> is the binding energy, n is the number of electrons transferred (n = 1 in our case), F is the Faraday constant, and E is the potential). The Na binding energy in perfect graphene was estimated as 0.49 eV, indicating that sodiation on the surface of perfect graphene required a large overpotential since the sodiation potential was -0.49 V vs. Na/Na<sup>+</sup>. In the graphitic-N/S and pyrrolic-N models, the binding energy ranged from 0.31 to 0.65 eV,

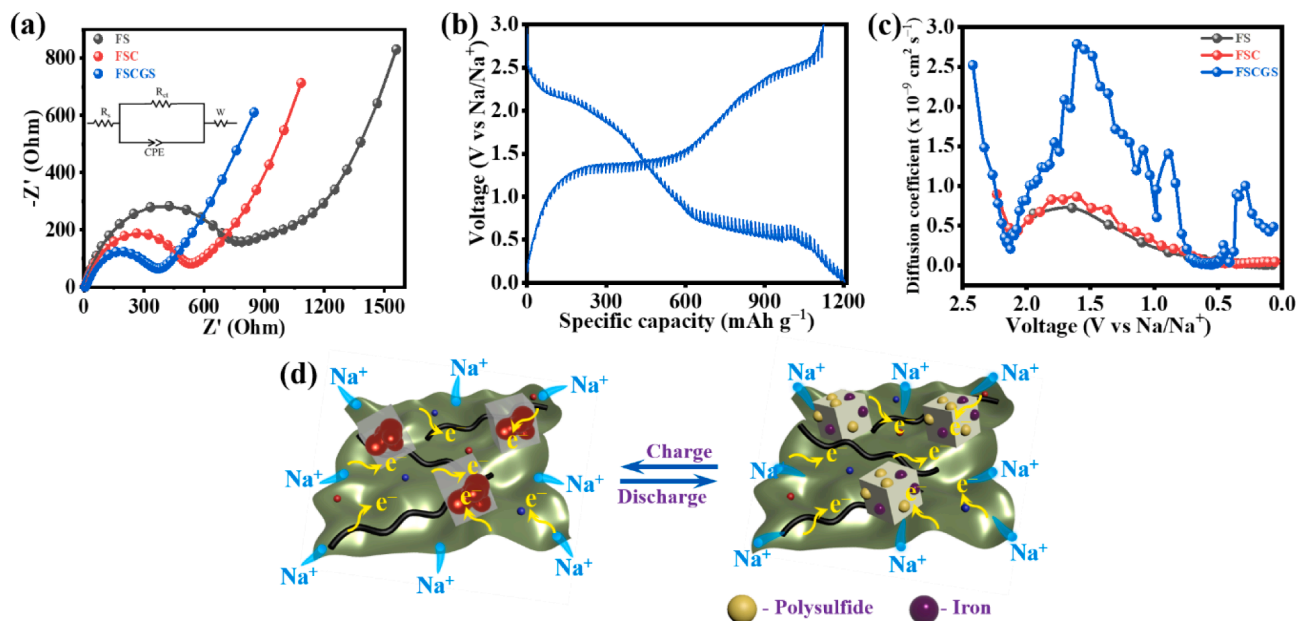


Fig. 5. (a) Electrochemical impedance spectra of the FS, FSC, and FSCGS samples after 200 cycles at  $1.0 \text{ A g}^{-1}$ . (b) Galvanostatic intermittent titration plot of the FSCGS sample. (c) Sodium-ion chemical diffusion coefficient plots of the FS, FSC, and FSCGS samples. (d) Schematic illustration of the Na-ion insertion/extraction mechanism during charging and discharging of the FSCGS sample.

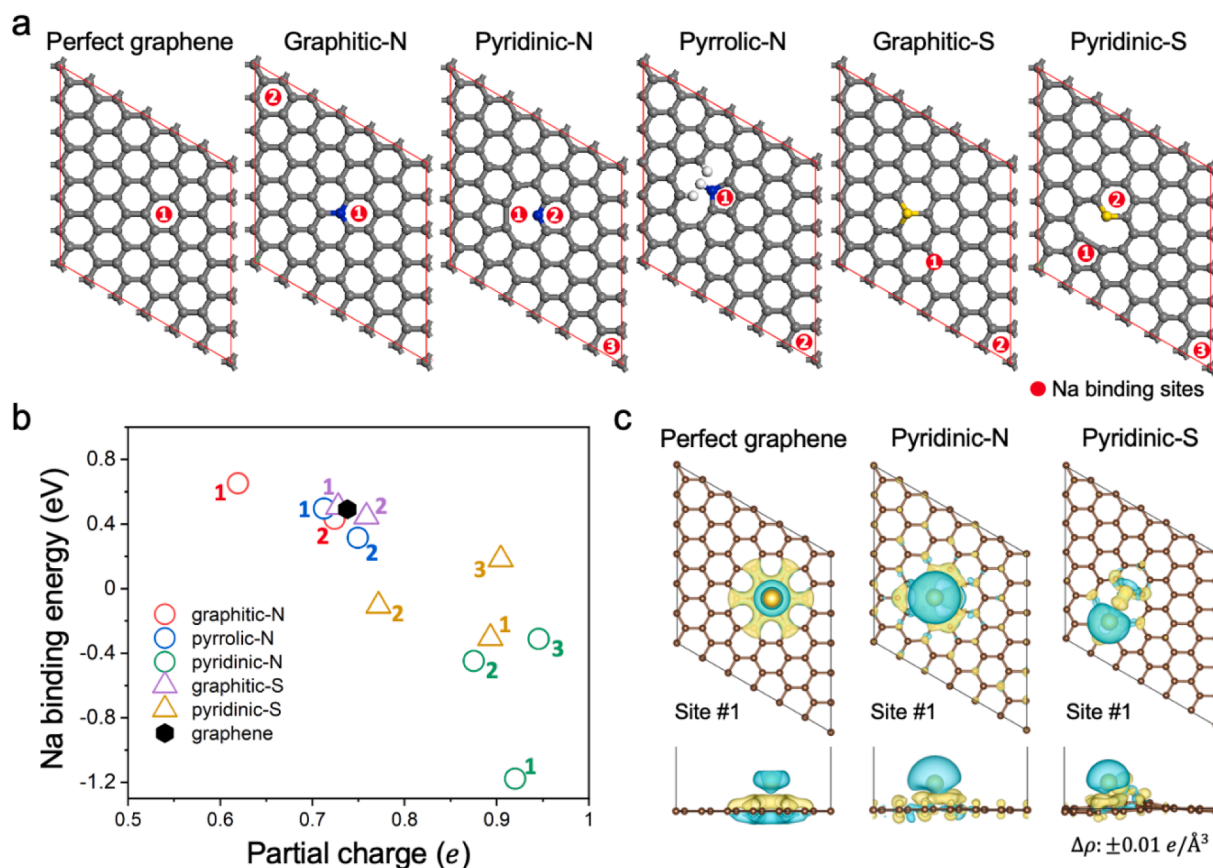


Fig. 6. (a) Perfect and various other N/S-doped basal graphene structures and Na binding sites. (b) Correlation between the Na binding energy and Bader partial charge of the Na atom. (c) Representative differential charge density map before and after Na binding.

depending on the binding sites. Thus, there was no significant difference in binding energy compared with perfect graphene. On the other hand, the pyridinic-N/S models exhibited significantly improved binding

energy compared with perfect graphene (pyridinic N:  $-1.18$  to  $-0.31$  eV; pyridinic S:  $-0.31$  to  $0.18$  eV). In the latter case, binding was strongest to the defect site (five-membered-ring site) formed adjacent to

the doping site; the binding weakened with increasing distance from the doping site. However, considering that the binding energy was significantly improved compared with perfect graphene at the six-membered ring site farthest from the doping site, it was concluded that pyridinic-N/S doping not only provided a strong local binding site but also improved the sodiation performance of the entire graphene basal plane.

The mechanism of enhanced Na binding upon pyridinic-N/S doping was investigated using Bader partial charge analysis. Fig. 6b shows that the partial charge of adsorbed Na and its binding energy were strongly correlated. In perfect graphene, adsorbed Na has a partial charge of 0.74, and every pyridinic-N/S site with significantly enhanced binding energy had higher oxidation states with partial charge ranging from 0.77 to 0.98. In contrast, the rest of the structures, with Na binding energies similar to that of perfect graphene, had partial charges in the range of 0.62–0.76. This is because changes in the local atomic and electronic structures due to pyridinic-N/S doping enhanced the uptake ability of additional electrons during reduction. Thus, Na was adsorbed in the stable monovalent oxidation state, which maximized Coulombic interaction between Na and the surface. Furthermore, the differential electron density analysis before and after Na adsorption (Fig. 6c and Fig. S19) revealed that additional electrons were localized near the pyridinic-N/S and binding sites. On the other hand, the perfect graphene structure had a much lower and more distributed differential electron density on the surface. These results suggest that the pyridinic form of N/S doping on the basal graphene network efficiently reduced the sodiation overpotential and was responsible for the enhanced experimental electrochemical performance.

### 3. Conclusion

We designed and synthesized N-doped carbon-coated FeS<sub>2</sub> nanoparticles encapsulated in N/S dual-doped G/SWCNT network composites and evaluated their utility as anodes for SIBs. The presence of carbon entities of N-doped carbon shells and an N/S dual-doped highly conductive G/SWCNT network significantly improved the active material's pseudocapacitive nature and electrical conductivity. It thus ensured excellent specific capacity and rate capability. The FSCGS sample exhibited a remarkable specific capacity of 1,190 mAh g<sup>-1</sup> at a current density of 0.1 A g<sup>-1</sup> with an excellent rate capability of 476 mAh g<sup>-1</sup> at 10.0 A g<sup>-1</sup>. Furthermore, the protection of FeS<sub>2</sub> by the nanorattle-structured N-doped carbon coating, as well as the N/S dual-doped G/SWCNT network, accommodated the volume expansion during charge/discharge cycles, which resulted in improved specific capacity retention of 91.3% at 0.5 A g<sup>-1</sup> and 83.6% at 1.0 A g<sup>-1</sup> after 200 cycles. Furthermore, first-principles calculations revealed that reducing the sodiation overpotential by pyridinic-N/S doping of the basal graphene network improved electrochemical performance. The current approach is a universal and promising solution that effectively maximizes the performance of active anode materials, which are difficult to apply in practice due to volume expansion and low electrical conductivity.

### Declaration of Competing Interest

The authors declare that they have no known competing financial interests or personal relationships that could have appeared to influence the work reported in this paper.

### Acknowledgment

This work was mainly supported by Brain Pool Program through the National Research Foundation of Korea (NRF), funded by the Ministry of Science and ICT (Grant no.2019H1D3A1A01070498). In addition, we also gratefully acknowledge financial support from the Korea Institute of Science and Technology (KIST) institutional and KU-KIST programs (Project No. 2E31811) and the National Research Foundation of Korea (NRF) grant funded by the Korea government (No.

2022R1A2B5B02001597 and 2018M1A2A2061994).

### Appendix A. Supplementary data

Supplementary data to this article can be found online at <https://doi.org/10.1016/j.cej.2022.135678>.

### References

- [1] Y. Liang, H. Dong, D. Aurbach, Y. Yao, Current status and future directions of multivalent metal-ion batteries, *Nat. Energy*. 5 (2020) 646–656, <https://doi.org/10.1038/s41560-020-0655-0>.
- [2] H.-H. Ryu, H.H. Sun, S.-T. Myung, C.S. Yoon, Y.-K. Sun, Reducing cobalt from lithium-ion batteries for the electric vehicle era, *Energy Environ. Sci.* 14 (2021) 844–852, <https://doi.org/10.1039/D0EE03581E>.
- [3] G. Assat, J.-M. Tarascon, Fundamental understanding and practical challenges of anionic redox activity in Li-ion batteries, *Nat. Energy*. 3 (2018) 373–386, <https://doi.org/10.1038/s41560-018-0097-0>.
- [4] Z. Yang, X. Liu, X. He, W. Lai, L. Li, Y. Qiao, S. Chou, M. Wu, Rechargeable sodium-based hybrid metal-ion batteries toward advanced energy storage, *Adv. Funct. Mater.* 31 (2021) 2006457, <https://doi.org/10.1002/adfm.202006457>.
- [5] B. Lee, E. Paek, D. Mitlin, S.W. Lee, Sodium metal anodes: emerging solutions to dendrite growth, *Chem. Rev.* 119 (2019) 5416–5460, <https://doi.org/10.1021/acs.chemrev.8b00642>.
- [6] P. Vassilaras, D.-H. Kwon, S.T. Dacek, T. Shi, D.-H. Seo, G. Ceder, J.C. Kim, Electrochemical properties and structural evolution of O<sub>3</sub>-type layered sodium mixed transition metal oxides with trivalent nickel, *J. Mater. Chem. A*. 5 (2017) 4596–4606, <https://doi.org/10.1039/C6TA09220A>.
- [7] J. Liao, C. Chen, Q. Hu, Y. Du, Y. He, Y. Xu, Z. Zhang, X. Zhou, A low-strain phosphate cathode for high-rate and ultralong cycle-life potassium-ion batteries, *Angew. Chemie Int. Ed.* 60 (2021) 25575–25582, <https://doi.org/10.1002/anie.202112183>.
- [8] L. Duan, Y. Xu, Z. Zhang, J. Xu, J. Liao, J. Xu, Y. Sun, Y. He, X. Zhou, A high-performance cathode for potassium-ion batteries based on uniform P<sub>3</sub>-type K<sub>0.5</sub>Mn<sub>0.8</sub>CO<sub>0.1</sub>Ni<sub>0.1</sub>O<sub>2</sub> porous microcuboids, *J. Mater. Chem. A*. 9 (2021) 22820–22826, <https://doi.org/10.1039/D1TA07108D>.
- [9] Y. Du, W. Weng, Z. Zhang, Y. He, J. Xu, J. Sun, J. Liao, J. Bao, X. Zhou, Candelabra-like architecture consisting of FeS<sub>2</sub>@C core-shell particles for efficient potassium storage, *ACS Mater. Lett.* 3 (2021) 356–363, <https://doi.org/10.1021/acsmaterialslett.1c00129>.
- [10] J. Wu, R. Zhang, Q. Fu, J. Zhang, X. Zhou, P. Gao, C. Xu, J. Liu, X. Guo, Inorganic solid electrolytes for all-solid-state sodium batteries: fundamentals and strategies for battery optimization, *Adv. Funct. Mater.* 31 (2021) 2008165, <https://doi.org/10.1002/adfm.202008165>.
- [11] Y. Zhu, S.H. Choi, X. Fan, J. Shin, Z. Ma, M.R. Zachariah, J.W. Choi, C. Wang, Recent progress on spray pyrolysis for high performance electrode materials in lithium and sodium rechargeable batteries, *Adv. Energy Mater.* 7 (2017) 1601578, <https://doi.org/10.1002/aenm.201601578>.
- [12] W.D. Richards, T. Tsujimura, L.J. Miara, Y. Wang, J.C. Kim, S.P. Ong, I. Uechi, N. Suzuki, G. Ceder, Design and synthesis of the superionic conductor Na<sub>10</sub>SnP<sub>2</sub>S<sub>12</sub>, *Nat. Commun.* 7 (2016) 11009, <https://doi.org/10.1038/ncomms11009>.
- [13] C. Yang, S. Xin, L. Mai, Y. You, Materials design for high-safety sodium-ion battery, *Adv. Energy Mater.* 11 (2021) 2000974, <https://doi.org/10.1002/aenm.202000974>.
- [14] T. Jin, Q. Han, L. Jiao, Binder-free electrodes for advanced sodium-ion batteries, *Adv. Mater.* 32 (2020) 1806304, <https://doi.org/10.1002/adma.201806304>.
- [15] Z. Jian, Z. Xing, C. Bommier, Z. Li, X. Ji, Hard carbon microspheres: potassium-ion anode versus sodium-ion anode, *Adv. Energy Mater.* 6 (2016) 1501874, <https://doi.org/10.1002/aenm.201501874>.
- [16] S.Y. Lim, J.H. Lee, S. Kim, J. Shin, W. Choi, K.Y. Chung, D.S. Jung, J.W. Choi, Lattice water for the enhanced performance of amorphous iron phosphate in sodium-ion batteries, *ACS Energy Lett.* 2 (2017) 998–1004, <https://doi.org/10.1021/acsenenergylett.7b00120>.
- [17] W. Weng, J. Xu, C. Lai, Z. Xu, Y. Du, J. Lin, X. Zhou, Uniform Yolk-shell Fe<sub>7</sub>S<sub>8</sub>@C nanoboxes as a general host material for the efficient storage of alkali metal ions, *J. Alloys Compd.* 817 (2020), 152732, <https://doi.org/10.1016/j.jallcom.2019.152732>.
- [18] B. Jache, P. Adelhelm, Use of graphite as a highly reversible electrode with superior cycle life for sodium-ion batteries by making use of co-intercalation phenomena, *Angew. Chemie Int. Ed.* 53 (2014) 10169–10173, <https://doi.org/10.1002/anie.201403734>.
- [19] C. Chen, Y. Yang, X. Tang, R. Qiu, S. Wang, G. Cao, M. Zhang, Graphene-encapsulated FeS<sub>2</sub> in carbon fibers as high reversible anodes for Na<sup>+</sup>/K<sup>+</sup> batteries in a wide temperature range, *Small*. 15 (2019) 1804740, <https://doi.org/10.1002/smll.201804740>.
- [20] J. Kim, M.S. Choi, K.H. Shin, M. Kota, Y. Kang, S. Lee, J.Y. Lee, H.S. Park, Rational design of carbon nanomaterials for electrochemical sodium storage and capture, *Adv. Mater.* 31 (2019) 1803444, <https://doi.org/10.1002/adma.201803444>.
- [21] K.C. Kim, T. Liu, K.H. Jung, S.W. Lee, S.S. Jang, Unveiled correlations between electron affinity and solvation in redox potential of quinone-based sodium-ion batteries, *Energy Storage Mater.* 19 (2019) 242–250, <https://doi.org/10.1016/j.ensm.2019.01.017>.

- [22] X. Xu, L. Si, X. Zhou, F. Tu, X. Zhu, J. Bao, Chemical bonding between antimony and ionic liquid-derived nitrogen-doped carbon for sodium-ion battery anode, *J. Power Sources*. 349 (2017) 37–44, <https://doi.org/10.1016/j.jpowsour.2017.03.026>.
- [23] M. Mao, F. Yan, C. Cui, J. Ma, M. Zhang, T. Wang, C. Wang, Pipe-Wire TiO<sub>2</sub>-Sn@Carbon nanofibers paper anodes for lithium and sodium ion batteries, *Nano Lett.* 17 (2017) 3830–3836, <https://doi.org/10.1021/acs.nanolett.7b01152>.
- [24] H. Su, S. Jaffer, H. Yu, Transition metal oxides for sodium-ion batteries, *Energy Storage Mater.* 5 (2016) 116–131, <https://doi.org/10.1016/j.ensm.2016.06.005>.
- [25] S. Kandula, J. Bae, J. Cho, J.G. Son, Gram-scale Synthesis of rGO wrapped porous  $\alpha$ -Fe<sub>2</sub>O<sub>3</sub> as an advanced anode material for na-ion batteries with superior cyclic stability, *Compos. Part B Eng.* 220 (2021), 108995, <https://doi.org/10.1016/j.compositesb.2021.108995>.
- [26] Z. Li, L. Zhang, X. Ge, C. Li, S. Dong, C. Wang, L. Yin, Core-shell Structured CoP/FeP porous microcubes interconnected by reduced graphene oxide as high performance anodes for sodium ion batteries, *Nano Energy*. 32 (2017) 494–502, <https://doi.org/10.1016/j.nanoen.2017.01.009>.
- [27] M. Sun, H. Liu, J. Qu, J. Li, Earth-rich transition metal phosphide for energy conversion and storage, *Adv. Energy Mater.* 6 (2016) 1600087, <https://doi.org/10.1002/aenm.201600087>.
- [28] Z. Man, P. Li, D. Zhou, Y. Wang, X. Liang, R. Zang, P. Li, Y. Zuo, Y.M. Lam, G. Wang, Two Birds with One Stone: FeS<sub>2</sub>@C yolk-shell composite for high-performance sodium-ion energy storage and electromagnetic wave absorption, *Nano Lett.* 20 (2020) 3769–3777, <https://doi.org/10.1021/acs.nanolett.0c00789>.
- [29] H. Yuan, F. Ma, X. Wei, J. Lan, Y. Liu, Y. Yu, X. Yang, H.S. Park, Ionic-conducting and robust multilayered solid electrolyte interphases for greatly improved rate and cycling capabilities of sodium ion full cells, *Adv. Energy Mater.* 10 (2020) 2001418, <https://doi.org/10.1002/aenm.202001418>.
- [30] Y. Fang, D. Luan, X.W. David Lou, Recent advances on mixed metal sulfides for advanced sodium-ion batteries, *Adv. Mater.* 32 (2020) 2002976, <https://doi.org/10.1002/adma.202002976>.
- [31] Y. Xiao, S.H. Lee, Y.-K. Sun, The application of metal sulfides in sodium ion batteries, *Adv. Energy Mater.* 7 (2017) 1601329, <https://doi.org/10.1002/aenm.201601329>.
- [32] Z. Hu, Z. Zhu, F. Cheng, K. Zhang, J. Wang, C. Chen, J. Chen, Pyrite FeS<sub>2</sub> for high-rate and long-life rechargeable sodium batteries, *Energy Environ. Sci.* 8 (2015) 1309–1316, <https://doi.org/10.1039/C4EE03759F>.
- [33] Y.-X. Wang, J. Yang, S.-L. Chou, H.K. Liu, W. Zhang, D. Zhao, S.X. Dou, Uniform yolk-shell iron sulfide-carbon nanospheres for superior sodium-iron sulfide batteries, *Nat. Commun.* 6 (2015) 8689, <https://doi.org/10.1038/ncomms9689>.
- [34] H.-H. Fan, H.-H. Li, K.-C. Huang, C.-Y. Fan, X.-Y. Zhang, X.-L. Wu, J.-P. Zhang, Metastable marcasite-FeS<sub>2</sub> as a new anode material for lithium ion batteries: CNFs-improved lithiation/delithiation reversibility and li-storage properties, *ACS Appl. Mater. Interfaces*. 9 (2017) 10708–10716, <https://doi.org/10.1021/acsami.7b00578>.
- [35] A. Huang, Q. Wang, Z. Ma, K. Rui, X. Huang, J. Zhu, W. Huang, Surface anionization of self-assembled iron sulfide hierarchitectures to enhance capacitive storage for alkaline-metal-ion batteries, *ACS Appl. Mater. Interfaces*. 11 (2019) 39991–39997, <https://doi.org/10.1021/acsami.9b13629>.
- [36] Q. Wang, W. Zhang, C. Guo, Y. Liu, C. Wang, Z. Guo, In situ Construction of 3D Interconnected FeS@Fe<sub>3</sub>C@Graphitic carbon networks for high-performance sodium-ion batteries, *Adv. Funct. Mater.* 27 (2017) 1703390, <https://doi.org/10.1002/adfm.201703390>.
- [37] M. Walter, T. Zünd, M.V. Kovalenko, Pyrite (FeS<sub>2</sub>) Nanocrystals as inexpensive high-performance lithium-ion cathode and sodium-ion anode materials, *Nanoscale*. 7 (2015) 9158–9163, <https://doi.org/10.1039/C5NR00398A>.
- [38] R. Hu, H. Zhao, J. Zhang, Q. Liang, Y. Wang, B. Guo, R. Dangol, Y. Zheng, Q. Yan, J. Zhu, Scalable Synthesis of a Foam-like FeS<sub>2</sub> Nanostructure by a solution combustion-sulfurization process for high-capacity sodium-ion batteries, *Nanoscale*. 11 (2019) 178–184, <https://doi.org/10.1039/C8NR06675B>.
- [39] R. Zang, P. Li, X. Guo, Z. Man, S. Zhang, C. Wang, G. Wang, Yolk-shell N-doped carbon coated FeS<sub>2</sub> nanocages as a high-performance anode for sodium-ion batteries, *J. Mater. Chem. A*. 7 (2019) 14051–14059, <https://doi.org/10.1039/C9TA03917A>.
- [40] P. Jing, Q. Wang, B. Wang, X. Gao, Y. Zhang, H. Wu, Encapsulating yolk-shell FeS<sub>2</sub>@carbon microboxes into interconnected graphene framework for ultrafast lithium/sodium storage, *Carbon* 159 (2020) 366–377, <https://doi.org/10.1016/j.carbon.2019.12.060>.
- [41] Z. Liu, T. Lu, T. Song, X.-Y. Yu, X.W. Lou, U. Paik, Structure-designed synthesis of FeS<sub>2</sub>@C yolk-shell nanoboxes as a high-performance anode for sodium-ion batteries, *Energy Environ. Sci.* 10 (7) (2017) 1576–1580.
- [42] M. Zhou, H. Tao, K. Wang, S. Cheng, K. Jiang, Nano-embedded microstructured FeS<sub>2</sub>@C as a high capacity and cycling-stable Na-storage anode in an optimized ether-based electrolyte, *J. Mater. Chem. A*. 6 (2018) 24425–24432, <https://doi.org/10.1039/C8TA05751A>.
- [43] Y. Ding, P. Zeng, Z. Fang, Spindle-shaped FeS<sub>2</sub> enwrapped with N/S Co-doped carbon for high-rate sodium storage, *J. Power Sources*. 450 (2020), 227688, <https://doi.org/10.1016/j.jpowsour.2019.227688>.
- [44] Y. Hao, X. Li, W. Liu, H. Maleki Kheimeh Sari, J. Qin, Y. Li, Asynchronous reactions of “self-matrix” dual-crystals effectively accommodating volume expansion/shrinkage of electrode materials with enhanced sodium storage, *Chem. Commun.* 55 (62) (2019) 9076–9079.
- [45] S. Kandula, K.R. Shrestha, G. Rajeshkhanna, N.H. Kim, J.H. Lee, Kirkendall growth and Ostwald ripening induced hierarchical morphology of Ni-Co LDH/MMO<sub>x</sub> (M = Co, Ni, and Zn) heteronanostructures as advanced electrode materials for asymmetric solid-state supercapacitors, *ACS Appl. Mater. Interfaces*. 11 (2019) 11555–11567, <https://doi.org/10.1021/acsami.9b02978>.
- [46] S. Kandula, K.R. Shrestha, N.H. Kim, J.H. Lee, Fabrication of a 3D hierarchical Sandwich Co<sub>9</sub>S<sub>8</sub>/α-MnS@N-C@MoS<sub>2</sub> nanowire architectures as advanced electrode material for high performance hybrid supercapacitors, *Small*. 14 (2018) 1800291, <https://doi.org/10.1002/smll.201800291>.
- [47] N. Voronina, H. Yashiro, S.-T. Myung, Marcasite iron sulfide as a high-capacity electrode material for sodium storage, *J. Mater. Chem. A*. 6 (2018) 17111–17119, <https://doi.org/10.1039/C8TA06312E>.
- [48] A. Douglas, R. Carter, L. Oakes, K. Share, A.P. Cohn, C.L. Pint, Ultrafine iron pyrite (FeS<sub>2</sub>) nanocrystals improve sodium-sulfur and lithium-sulfur conversion reactions for efficient batteries, *ACS Nano*. 9 (2015) 11156–11165, <https://doi.org/10.1021/acsnano.5b04700>.
- [49] S. Wang, Y. Jing, L. Han, H. Wang, S. Wu, Y. Zhang, L. Wang, K. Zhang, Y.-M. Kang, F. Cheng, Ultrathin carbon-coated FeS<sub>2</sub> nanooctahedra for sodium storage with long cycling stability, *Inorg. Chem. Front.* 6 (2019) 459–464, <https://doi.org/10.1039/C8QI01144C>.
- [50] F. Wang, W. Zhang, H. Zhou, H. Chen, Z. Huang, Z. Yan, R. Jiang, C. Wang, Z. Tan, Y. Kuang, Preparation of porous FeS<sub>2</sub>-C/RG composite for sodium ion batteries, *Chem. Eng. J.* 380 (2020), 122549, <https://doi.org/10.1016/j.cej.2019.122549>.
- [51] Z. Lu, Y. Zhai, N. Wang, Y. Zhang, P. Xue, M. Guo, B. Tang, D. Huang, W. Wang, Z. Bai, S. Dou, FeS<sub>2</sub> Nanoparticles embedded in N/S Co-doped porous carbon fibers as anode for sodium-ion batteries, *Chem. Eng. J.* 380 (2020), 122455, <https://doi.org/10.1016/j.cej.2019.122455>.
- [52] M. Shao, Y. Cheng, T. Zhang, S. Li, W. Zhang, B. Zheng, J. Wu, W.-W. Xiong, F. Huo, J. Lu, Designing MOFs-derived FeS<sub>2</sub>@Carbon composites for high-rate sodium ion storage with capacitive contributions, *ACS Appl. Mater. Interfaces*. 10 (2018) 33097–33104, <https://doi.org/10.1021/acsami.8b10110>.
- [53] K.R. Shrestha, S. Kandula, G. Rajeshkhanna, M. Srivastava, N.H. Kim, J.H. Lee, An advanced sandwich-type architecture of MnCo<sub>2</sub>O<sub>4</sub>@N-C@MnO<sub>2</sub> as an efficient electrode material for a high-energy density hybrid asymmetric solid-state supercapacitor, *J. Mater. Chem. A*. 6 (2018) 24509–24522, <https://doi.org/10.1039/c8ta08976k>.
- [54] Y. Lu, K.H. Shin, Y. Yu, Y. Hu, J. Liang, K. Chen, H. Yuan, H.S. Park, D. Wang, Multiple active sites carbonaceous anodes for Na<sup>+</sup> storage: synthesis, electrochemical properties and reaction mechanism analysis, *Adv. Funct. Mater.* 31 (2021) 2007247, <https://doi.org/10.1002/adfm.202007247>.
- [55] C. Zhou, A. Li, B. Cao, X. Chen, M. Jia, H. Song, The non-ignorable impact of surface oxygen groups on the electrochemical performance of N/O dual-doped carbon anodes for sodium ion batteries, *J. Electrochem. Soc.* 165 (2018) A1447–A1454, <https://doi.org/10.1149/2.1061807jes>.
- [56] Z. Lin, X. Xiong, M. Fan, D. Xie, G. Wang, C. Yang, M. Liu, Scalable synthesis of FeS<sub>2</sub> nanoparticles encapsulated into n-doped carbon nanosheets as a high-performance sodium-ion battery anode, *Nanoscale*. 11 (2019) 3773–3779, <https://doi.org/10.1039/C8NR10444A>.
- [57] J. Choi, S.U. Yoon, M.E. Lee, S.I. Park, Y. Myung, H.-J. Jin, J.B. Lee, Y.S. Yun, High-performance nanohybrid anode based on FeS<sub>2</sub> nanocubes and nitrogen-rich graphene oxide nanoribbons for sodium ion batteries, *J. Ind. Eng. Chem.* 81 (2020) 61–66, <https://doi.org/10.1016/j.jiec.2019.08.059>.
- [58] X. Xu, J. Liu, Z. Liu, J. Shen, R. Hu, J. Liu, L. Ouyang, L. Zhang, M. Zhu, Robust pitaya-structured pyrite as high energy density cathode for high-rate lithium batteries, *ACS Nano*. 11 (2017) 9033–9040, <https://doi.org/10.1021/acsnano.7b03530>.
- [59] Z. Hu, Q. Liu, W. Sun, W. Li, Z. Tao, S.-L. Chou, J. Chen, S.-X. Dou, MoS<sub>2</sub> with an intercalation reaction as a long-life anode material for lithium ion batteries, *Inorg. Chem. Front.* 3 (2016) 532–535, <https://doi.org/10.1039/C5QI00237K>.
- [60] K. Zhang, Z. Hu, X. Liu, Z. Tao, J. Chen, FeSe<sub>2</sub> microspheres as a high-performance anode material for Na-ion batteries, *Adv. Mater.* 27 (2015) 3305–3309, <https://doi.org/10.1002/adma.201500196>.